Engineering 57 (2026) 189–199

Contents lists available at ScienceDirect

Engineering

journal homepage: www.elsevier.com/locate/eng

Research
Robotics—Article

Multi-Frequency Dual-Echo Magnetic Resonance Imaging for Real-Time and Artifact-Free Magnetic Robot Navigation

Renkuan Zhai [a,b,#], Zhangqi Pan [a,#], Yuanshi Kou [a], Chuang Yang [b], Yang Ruan [b], Chenli Xu [b], Linjie He [a], Jianfeng Zang [a,c,*]

[a] School of Integrated Circuits & Wuhan National Laboratory for Optoelectronics, Huazhong University of Science and Technology, Wuhan 430074, China
[b] Wuhan United Imaging Life Science Instrument, Wuhan 430206, China
[c] The State Key Laboratory of Intelligent Manufacturing Equipment and Technology, Huazhong University of Science and Technology, Wuhan 430074, China

ARTICLE INFO

Article history:
Received 21 September 2024
Revised 25 April 2025
Accepted 30 April 2025
Available online 1 July 2025

Keywords:
Real-time MRI navigation
Magnetic robot
Multi-frequency dual-echo sequence
Artifact-free
Precise control

ABSTRACT

Magnetic resonance imaging (MRI) systems, outfitted with internal gradient coils capable of manipulating magnetic gradients in three-dimensional (3D) space, offer an intriguing platform for the navigation of medical magnetic robots. These robots offer considerable promise for applications in minimally invasive therapy, targeted drug delivery, and theranostic interventions. However, an MRI-driven robot presents a challenging contradiction between real-time control and image resolution, resulting in suboptimal tracking accuracy—attributed to the inefficiency of conventional signal acquisition and the presence of metal artifacts. In this paper, we report a multi-frequency excitation sequence with dual-echo (MFDE) that reduces the repetition time (TR) to 30 ms, allowing the precise tracking of magnetic particles (relative error < 1%) without artifacts. The duty cycle of the driving gradient is as high as 77%, and perturbations from the imaging gradients are eliminated. Expanding on these foundations, we adapted our technique to 3D operations. We established an integrated platform for imaging and motion control by creating a three-view window and developing a control joystick to be used in conjunction with the platform. Demonstrations of navigation in a maze, in a phantom vessel, and *in vivo* animal trials validate its feasibility and effectiveness, providing a significant advancement in the field of MRI-guided magnetic robot control.

© 2025 THE AUTHORS. Published by Elsevier LTD on behalf of Chinese Academy of Engineering and Higher Education Press Limited Company. This is an open access article under the CC BY license (http://creativecommons.org/licenses/by/4.0/).

1. Introduction

Magnetic microrobots offer significant potential for application in minimally invasive or noninvasive precision therapies owing to their small size, high flexibility, and targeting ability [1–6]. The gradient magnetic field generated by magnetic resonance imaging (MRI) equipment can be used for both the phase and frequency encoding of the magnetic signals of hydrogen atoms in living organisms and for exerting gradient forces to control the locomotion of microrobots [3,7–11]. Developing magnetic resonance sequences is crucial for successfully integrating imaging and motion control in interventional surgery. One of the numerous advancements in magnetic-resonance-based steering techniques involves harnessing the gradient magnetic field to guide magnetic particles along intricate paths [11–18], which has shown remarkable precision in navigating magnetic robots through complex anatomical structures, such as in the delivery of thermal robots for ablative therapy [3] or in the precise targeted delivery of drugs to specific tissues [19,20].

Numerous studies [16–26] have focused on obtaining the center coordinates of magnetic robots using one-dimensional (1D) projections of MRI data to enhance the precision of magnetic particle tracking and motion control. Thereafter, the data are used to implement closed-loop control by applying control algorithms. The most prevalent of these control algorithms are proportional–integral–derivative (PID) control, error-state linear quadratic regulator (LQR), enhanced linear state observer (ELSO), generalized predictive control (GPC), and sliding mode control (SMC) algorithms [16,17,21–25], which compensate for errors caused by environmental factors. These approaches employ intelligent algorithms

* Corresponding author.
E-mail address: jfzang@hust.edu.cn (J. Zang).
# These authors contributed equally to this work.

https://doi.org/10.1016/j.eng.2025.04.027
2095-8099/© 2025 THE AUTHORS. Published by Elsevier LTD on behalf of Chinese Academy of Engineering and Higher Education Press Limited Company.
This is an open access article under the CC BY license (http://creativecommons.org/licenses/by/4.0/).

instead of manual control and omit two-dimensional (2D) imaging, thereby reducing the time required for MRI sequencing. However, in actual medical scenarios, the state of a robot is subject to considerable uncertainty because of its inability to fully model the effects of its complex physical environment [26]. Thus, incorporating real-time manual intervention into the navigation process, which necessitates the acquisition of high-resolution images without artifacts of the working area, is essential.

Traditional MRI sequences require substantial repetition time (TR = ~1000 ms) to acquire signals and produce clear images, resulting in a delay in the application of gradient forces to the image output [14,19,26]. For comparison, the time resolution limit of the human eye is only in the tens of milliseconds [27], shorter than this imaging delay of 1000 ms. Furthermore, a long imaging time results in a low-duty cycle for the control gradient. Some studies have attempted to shorten the sequence time by employing optimized fast low-angle shot (FLASH) pulse sequences and rapid acquisition with relaxation enhancement (RARE) sequences, achieving TRs as short as hundreds of milliseconds [26,28,29]. However, owing to steady-state spin magnetization [8], reducing the TR also reduces the quantity of data being collected to an insufficient amount, thus compromising imaging quality. Moreover, conventional sequences adopt a spoiler gradient at the end of each cycle as the motion driver, which signifies that imaging and motion control are operated alternately. Therefore, the gradient during the imaging process may also influence robot motion [16].

In this paper, we present an integrated MRI platform for real-time and artifact-free magnetic robot navigation (Fig. 1). We propose a multi-frequency and dual-echo (MFDE) sequence complemented by a reconstruction algorithm, reducing TR to a minimum of 30 ms with artifact-free background imaging, thus achieving precise positioning with less than 1% relative error, improving the duty cycle of the driving force to approximately 77%, and eliminating the effect of the imaging-related gradient on motion. To overcome the technical limitations associated with the long TR of imaging, two adjacent 180° radio-frequency (RF) pulses are employed to generate dual-echoes. The first 180° RF, analogous to a conventional spin-echo (SE) sequence, is employed to reverse the spin state of the proton, thereby achieving phase inversion. The other 180° RF is used for refocusing, enabling the spin to rapidly revert to its initial-state. In addition, the alternating positive and negative offset frequency excitation design circumvents the low-signal-intensity problem caused by the steady-state. To achieve artifact-free imaging, a high-resolution background image is obtained at the fundamental frequency, which is fixed during navigation. The real-time coordinates of the robot are calculated using offset frequency projection and reconstructed as a spot on the background. Through three-view image feedback and the incorporation of a control joystick, operators can manipulate a magnetic robot within the patient body, creating favorable conditions for the clinical application of this technology.

2. Materials and methods

2.1. MFDE sequence for real-time navigation

A MFDE sequence based on SE is shown in Fig. 2(a) (the TR limit is 30 ms, i.e., 33 frames per second (FPS)). In each sequence cycle, excitations at positive (pink) and negative (blue) offset frequencies (relative to the eigenfrequency of the proton spin procession) are adopted in an alternating manner. Two adjacent 180° RF pulses are applied to generate dual refocusing echoes. The driving forces in the sequence, marked in purple and green, are categorized into either "crushers" or "spoilers," respectively. Unlabeled graphs marked in gray indicate imaging gradients for the conventional SE sequence. A "spoiler" is used to eliminate interference during two adjacent repetitions. Additionally, because the effect of two gradients in the k-space is eliminated by the 180° refocusing RF in their middle, the gradients symmetrically on both sides of the 180° RF ("crushers") do not influence the imaging. Moreover, to eliminate the influence of the imaging gradients on the robot motion in the non-driven axes, we implement opposite gradients on each side of the two refocusing 180° RFs, as indicated by the yellow gradient. In a 30 ms sequence cycle, the total duration of imaging gradients and RF pulses is 6.9 ms. Thus, approximately 77% of the gradient fields can be allocated for magnetic steering (Table S1 in Appendix A).

One of the reasons for the reduction in the TR of the MFDE sequence to real time is the action of two adjacent 180° RFs to generate a dual-echo (Fig. 2(b)). Flip angle (α°) RF excitation results in the projection of a portion of magnetization onto the Z-axis (M_Z). The first 180° RF is similar to that of a conventional SE sequence, flipping the spin phase of the proton in k-space (comprising the flipping of the M_Z intensity; Note S1 in Appendix A). However, in a conventional SE sequence, the proton spin must return to its initial-state naturally before the next round of excitation can commence (as indicated by the gray dashed line), thus necessitating a longer TR. Adding a second 180° RF enables the proton spin to flip back, thereby accelerating the process of returning to the initial-state (gray solid line).

Another rationale behind the ability of the MFDE sequence to acquire high-intensity signals in finite time is related to the statistical spin-state recovery of protons [8], where the positive and negative offset frequencies excite protons situated at varying locations within the excitation volume. As shown in Fig. 2(c), following positive offset excitation, the protons in the corresponding space enter a steady-state (pink dotted box) and require an adequate relaxation time to recover their initial disordered spin state when not excited. Subsequently, the same excitation will result in a low signal intensity. This phenomenon is the origin of the low signal intensity observed in traditional imaging and tracking sequences and limits the TR. In this instance, the utilization of negative offset excitation ensures that the signal intensity is generated by the unexcited protons in the corresponding space (blue dotted box), which allows protons in the corresponding space of the positive offset excitation to recover the initial disordered spin state from the steady-state, thereby guaranteeing a high-intensity signal in the next cycle. Consequently, the use of alternating positive/negative offset excitation serves to greatly reduce the TR from the magnetic resonance mechanism of the nucleus while enhancing the signal intensity.

At the fundamental frequency, the distorted magnetic field around the magnetic particle appears black (Fig. 3(a)). The frequency offset curves are shown in Fig. 3(b), and the excitation intensities of the magnetic particles at the offset frequencies are shown in Fig. 3(c). The signal intensities of the MDFE sequences acquired within 30 ms were approximately 3–5 orders of magnitude (3–5 times the grayscale value) greater than that of a conventional fast SE (FSE) sequence. The MRI parameters for both the MFDE and FSE sequences were set to TR = 30 ms, echo time (TE) = 6 ms, flip angle (α°) = 10°, field of view (FOV) = 50 mm × 50 mm, and resolution = 256 × 256 pixels. The echo train length (ETL) of the FSE sequence was set to 4. The tests were conducted using an MRI scanner (uMR 9.4T, United Imaging Life Science Instrument, China). The magnetic robot utilized here was a 0.5 mm-diameter Fe particle (Fig. S1 in Appendix A).

To determine the specific value of the offset frequency, we measured the signal intensities and carrier-to-noise ratios (CNR) of magnetic particles at different frequencies, as shown in Figs. 3(d) and (e). The vertical direction (parallel to the MRI cavity) was excited with a positive frequency of +2500 Hz, whereas the

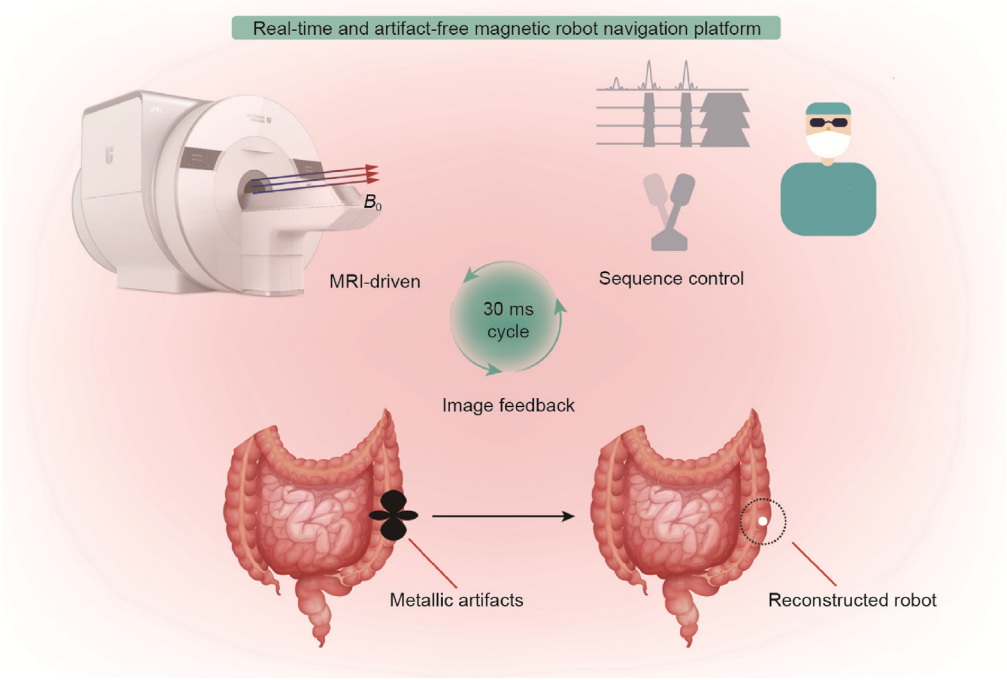

Fig. 1. Concept of real-time and artifact-free MRI-driven robot navigation platform. The integration of robotic drive and imaging feedback is implemented using MRI sequences. The entire cycle time is reduced to 30 ms for real-time navigation, and the introduction of reconstruction algorithms enables the removal of artifacts. B_0: the main magnetic field.

horizontal direction was excited with a negative frequency of −2000 Hz for high CNR. The obtained image highlights only the magnetic characteristic curve of the specific frequency, whereas the other parts of the offset frequency appear black. Thus, the centers of the symmetric bright arcs can be calculated to determine the coordinates. Notably, the MRI scanning process can be subject to various forms of interference. Therefore, selecting an offset frequency with a high signal-to-noise ratio and high intensity is a prerequisite for achieving precise tracking. In addition, the main field B_0 of the MRI equipment should be fully homogenized before the start of the experiment to prevent the occurrence of interfering signals.

2.2. Reconstruction algorithm for artifact-free background imaging and precise robot tracking

In the previous section, we addressed the challenge of real-time imaging and control through sequence innovation. Next, we eliminate the artifacts by designing a reconstruction algorithm to accompany the MFDE sequence to improve image quality and increase the precision of magnetic robot tracking (Fig. 4(a)). First, the background is imaged alone without the magnetic robot. For clear background imaging, the sequence used is an FSE sequence, as shown in Fig. 4(b).

Subsequently, the robot is delivered into the experimental environment. Based on the MFDE sequence, the frequency features around the magnetic robot are projected onto the *X*-, *Y*-, and *Z*-axes using offset frequency excitation. Fig. 4(c) shows the signal intensity distribution of the offset frequency images. The results of the 1D projection are used to calculate the position coordinates of the magnetic robot, as shown in Fig. 4(a). The midpoint of the integral intensity distribution is considered the coordinate. Notably, the magnetization direction of the magnetic particles is parallel to the main magnetic field of the MRI, resulting in rotational symmetry along the *Z*-axis for the offset frequency curves. Consequently, the coordinates in the *X*- and *Y*-directions can be projected simultaneously using positive offset excitation, whereas the *Z*-coordinates can be projected using negative offset excitation, thereby enabling 3D tracking.

Finally, a reconstruction algorithm is coded to draw a bright spot with the same shape and size as those of the magnetic robot on the fixed background obtained previously. Therefore, the artifacts can be replaced with spots according to the calculated position in the reconstructed image (Fig. 4(a)), and the magnetic robot replaced by the bright spot is updated in real time for precise control. The reconstruction (data computation) and sequencing (data acquisition) are run in parallel. Accordingly, the reconstruction time does not result in a delay in the output image, provided it is less than the sequence period. Considering our sequence circumvents the acquisition of superfluous signals, the requisite data computation is markedly reduced, culminating in a reconstruction time of only 1 μs.

Experiments were conducted to evaluate the accuracy of the calculated coordinates of the magnetic particle. Circular slots (diameter: 0.5 mm) were set to snap out the magnetic particle (Fig. S2 in Appendix A). The magnetic particle was fixed at different positions, and its coordinates were calculated using the imaging and reconstruction methods described previously, and compared with the setting coordinates. The average error of the magnetic particle in the *X*-direction was 0.24 mm, and in the *Z*-direction 0.14 mm (Fig. 4(d)). Comparing this deviation with the size of the imaging area, the average relative error was as low as 1%.

2.3. Dynamic model for MRI navigati

In an actual medical process, depending on the characteristics of the path and tasks to be performed, the forces acting on the magnetic robot must be constrained to achieve the desired motion. We model the kinematic laws of the magnetic robot in liquid and establish differential equations for velocity and time. Because the magnetic particle is spherical, the frictional force at the interface is small and can be neglected. The velocity–time differential

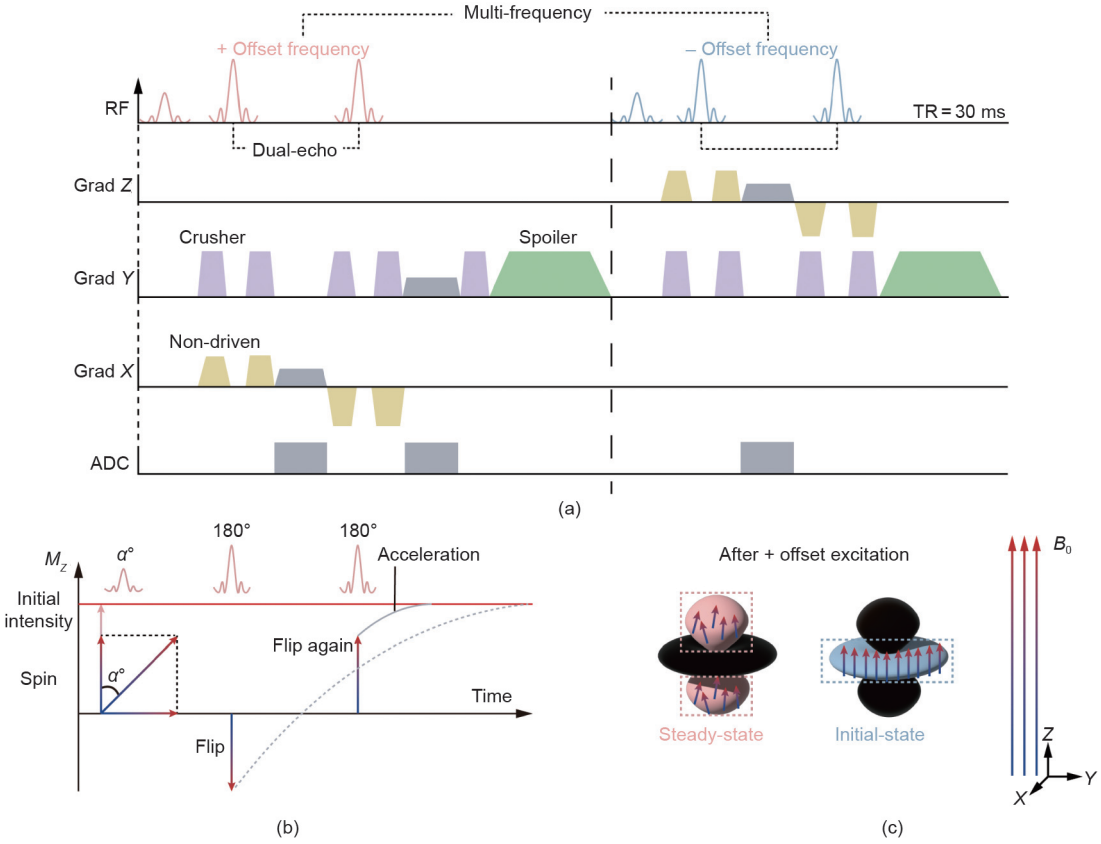

Fig. 2. Mechanism of MFDE sequence for real-time MRI navigation. (a) Schematic of MFDE sequence. Multi-frequency: in each cycle of the sequence, positive ("+" marked in pink) and negative ("–" marked in blue) offset frequencies are adopted alternately. Dual-echo: adjacent 180° RF pulses generate dual-echoes. Different gradient types are marked in different colors. ADC: analog to digital converter. (b) Effects of dual-echo. After flip angle (α°) RF excitation, a portion of magnetization is projected onto the *Z*-axis (M_Z). The first 180° RF flips M_Z, similar to that done in the common fast SE (FSE) sequence, where the recovery of M_Z to its initial intensity would be a relatively prolonged process. However, the second 180° RF flips it again, thereby accelerating the process. The TR is reduced as a result. The flipping of M_Z can be explained by the flipping or proton spin. Gray dashed and solid lines denote the magnetization intensity recovery curves with and without dual 180° excitation, respectively. (c) Effects of multi-frequency. After positive offset excitation, the protons in the corresponding space enter a macroscopic steady-state. Re-excitation before returning to the initial-state leads to low signal intensity. This situation can be circumvented by utilizing negative offset excitation. Similarly, the steady-state phenomenon occurs after negative offset excitation. Alternating +/– offset excitations overcome the signal intensity attenuation caused by the steady-state. Pink and blue dotted line boxes denote +/– offset excitation volumes, respectively.

equation, shown in Eq. (1) [20], expresses the motion in an infinite extent of fluid. The drag force ($D = \frac{1}{2}\rho_f C_d A_t u^2$), ρ_f is a function of the fluid density, C_d is drag efficiency, A_t is frontal area, and u is relative velocity. The drag efficiency C_d (the approximate value is taken as $C_{d\infty}$) is a function of *Re*, as shown in Eq. (2). Reynolds number *Re* is defined as in Eq. (3), where d is the diameter, m is the mass of the robot, t is time, and μ denotes the viscosity of the liquid.

$$F - \frac{1}{2}\rho_f C_d A_t u^2 = m\frac{du}{dt} \tag{1}$$

$$C_{d\infty} = \frac{24}{Re} + \frac{6}{1+\sqrt{Re}} + 0.4 \tag{2}$$

$$Re = \frac{\rho_f u d}{\mu} \tag{3}$$

where F denotes the driving force. In our work, the force is generated by the gradient coils of the MRI instrument and defined as shown in Eq. (4), where τ_m denotes the percentage of the magnetic volume to the volume V of the robot, $\vec{M}$ denotes the magnetization of the robot, ∇ is the gradient operator, and $\vec{B}$ is the magnetic induction intensity of the gradient field.

$$\vec{F} = \tau_m V(\vec{M}\cdot\nabla)\vec{B} \tag{4}$$

We solved the differential equation to obtain the velocity–time relationship curve (Fig. S3 in Appendix A). Theoretical analysis shows that under a consistent force magnitude, the magnetic robot undergoes a period of rapid acceleration and then maintains uniform motion. Considering the acceleration time is short, the entire motion process can be approximated to be uniform motion. Therefore, we can further establish the correspondence between the gradient force and average velocity.

We conducted experiments to obtain the position–time relationship. Different gradients and durations were applied to the magnetic robot in a liquid environment to simulate different viscosities of the human body. The viscosity of blood in different parts of the human body is approximately 3–5 times that of water, and the maximum viscosity of intestinal solution can reach 8–10 times that of water. The displacement–time relationship of the magnetic robot moving in liquids with different viscosities and under different gradient forces is shown in Fig. 5(a) and Fig. S4 in Appendix A. Fig. 5(b) shows the average speeds of magnetic robots in different viscosities and with different magnetic gradients. The viscosities of the liquids can be modified by varying the water-to-glycerin ratio. To demonstrate the ability of the MFDE sequence to precisely control the velocity of the magnetic robot, we designed a bifurcated path as shown in Fig. 5(c). Owing to the real-time feedback from imaging to control, the driving force can be changed instantaneously as the robot passes through the bifurcation. The robot is controlled to move in the direction of the two arrows in the figure

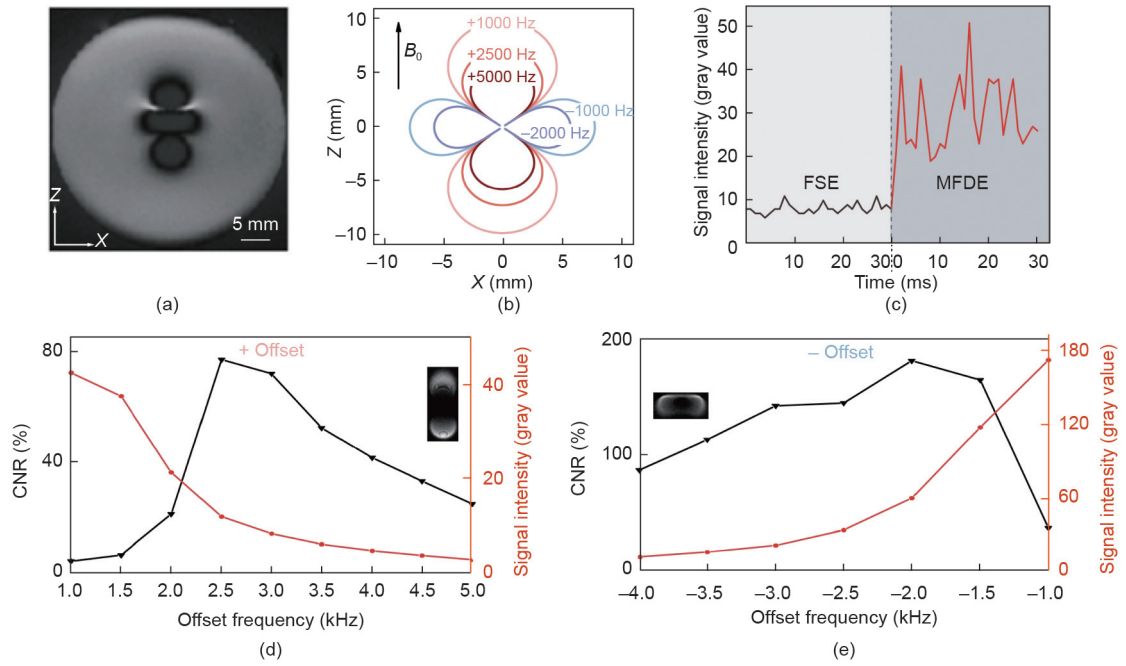

Fig. 3. Characterization of the MFDE sequence. (a) Distorted magnetic field around magnetic particles (spherical Fe particles) at the fundamental frequency. (b) Frequency offset curves corresponding to the +/− offsets. (c) Offset frequency excitation intensity contrast of the conventional FSE and MFDE sequences. (d, e) Carrier-to-noise ratios (CNR) and signal intensities of (d) positive offset and (e) negative offset frequency excitation. Images under positive/negative offset frequency excitation are shown in (d) and (e), respectively. The saturation magnetization of Fe is 1.73×10^6 A·m^{-1}, and the diameter of the particle is 0.5 mm.

at velocities V_1 and V_2, as shown in Fig. 5(d). The main magnetic field of up to 9.4 Tesla (T) provides a significantly enhanced driving force, enabling control over the robots even with low magnetization (Fig. S5 in Appendix A). At magnetic particle diameters of 0.3–0.8 mm, reductions in signal strength and signal-to-noise ratio occurred, resulting in minor increases in positioning accuracy error. Furthermore, at high viscosities with the same driving force, the velocities of the magnetic particles decrease as the particles become smaller. Overall, the reduction in the magnetic properties of the material has a negligible effect on the navigation process.

3. Results and discussion

3.1. Integrated real-time navigation platform and maze navigation demonstration

This section presents a demonstration of the proposed platform for real-time open-loop navigation. Building on the aforementioned MFDE sequences, reconstruction methods, and kinetic parameter modeling, we constructed an integrated imaging-control platform. Three-dimensional (3D) visual feedback is provided through three views. Input is provided via a joystick, which allows operators to adjust the driving force on demand.

For the navigation demonstration, a maze comprising three levels was designed using SolidWorks (Dassault Systemes, USA) and 3D-printed using polylactic acid (PLA) material. The 3D maze consisted of upper and lower structures, with a vertical path between the two layers (Fig. S6 in Appendix A). First, the maze was filled with water. Then, an FSE sequence was used to obtain images of the maze at each level in the coronal, sagittal, and transverse positions to generate a 3D image of the spatial background, which was to be employed for navigation by the magnetic robot. The layer thickness of the image was determined by the size of the robot. In this instance, we used 0.5 mm-diameter spherical Fe particles; thus, the layer thickness was established to be approximately 0.5 mm.

The magnetic robot could be steered to move along an arbitrary path within the maze, as illustrated in Fig. 6(a). The position of the magnetic robot within the 3D space of the maze is shown on the Windows client display, which includes a stereoscopic image and a three-view image (the coronal, transverse, and sagittal images are labeled with their corresponding abbreviations Cor., Tra., and Sag., respectively). The three-view image is continuously updated with the real-time position of the magnetic robot. To illustrate, as the robot progresses from the bottom layer to the upper layer within the maze, the coronal views are updated, and the various coronal images from the bottom to upper layers are presented as different levels of the maze, as depicted in the diagram shown in Fig. 6(b). At the client, the magnetic gradient force applied to the magnetic robot is determined via a Microsoft Foundation Class (MFC) control panel (Fig. S7(a) in Appendix A) and conveyed to a Linux server, which oversees the MRI apparatus via socket communication. Subsequently, the server calculates the gradient sizes of G_X, G_Y, and G_Z in accordance with the magnitude of the force in the three directions (Eq. (4)). Additionally, a joystick compatible with the control panel is developed; this joystick features knobs for adjusting the magnetic gradient force in the *X*-, *Y*-, and *Z*-directions and the conversion ratio (Fig. S7(b) in Appendix A). The forces in the three directions are updated in real time, and the MFDE parameters of the sequence are modified accordingly. The real-time control and imaging of the magnetic robot is thus completed, and the results are fed back to the user end, forming an open-loop control process.

The magnetic robot was guided through a complex structure at the bottom of the maze. The speed and direction of movement can be modified in real time, ensuring stable and efficient control. A real-time analysis of the position and velocity of the robot can be employed as feedback (Fig. 6(c)). The navigation routes in each layer are shown in Figs. 6(d)–(f). Controlling the motion of the robot in the vertical direction represents a significant challenge for 3D control, largely because of the buoyancy of the liquids (such as blood, cerebrospinal fluid, and other physiological internal fluids) in which the robot is operated. To address this challenge, providing real-time image feedback and precise tracking is crucial

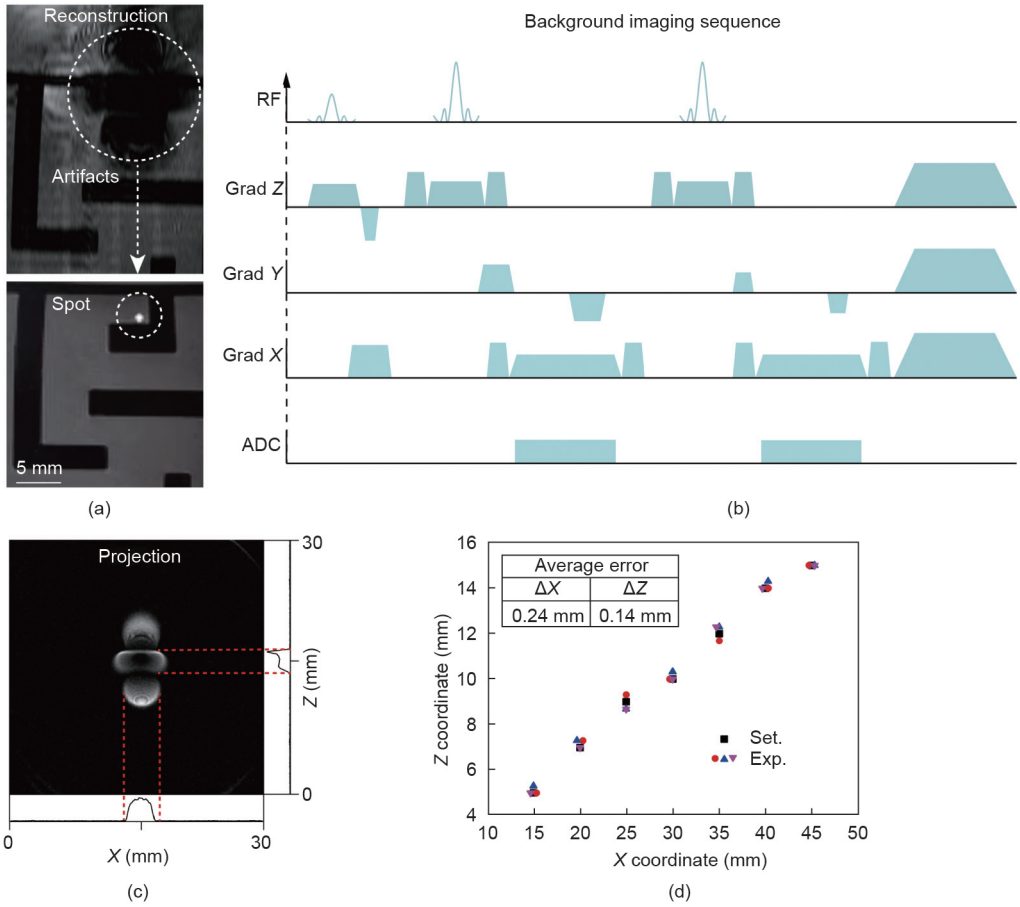

Fig. 4. Artifact-free image reconstruction techniques for high-resolution imaging and precise tracking. (a) Schematic of reconstruction technique, which replaces magnetic robot artifacts with bright spots on a pre-obtained background. (b) Schematic of FSE sequence for high-resolution imaging as the fixed background. (c) Projected signal distribution of offset frequency images for robot tracking. The center of the symmetric distribution of luminance can be considered as the three-dimensional (3D) coordinates of the magnetic robot, where the *X* and *Y* coordinates are simultaneously obtained from the positive offset frequency, and the *Z* coordinates are obtained from the negative offset frequency. (d) Spot position accuracy analysis. The positions of the magnetic particles were restricted by a mold with circular slots, and the geometric positions of the slots, considered as the setting coordinates, were compared with the experimentally calculated values to have a relative error of approximately only 1%. Set.: setting coordinate; Exp.: experiment.

to enable rapid correction of the applied magnetic gradient force in the *Y*-direction. As illustrated in Fig. 6(e), the transition in the passage between the bottom and upper layers indicates that our proposed control method exhibits high accuracy and stability in the vertical direction. Once the robot reached the upper endpoint (Fig. 6(f)), the entire experiment was concluded. Demonstration experiments were conducted with TRs of 30 and 100 ms for an intuitive sense of real-time control (Videos S1 and S2 in Appendix A). As mentioned earlier, 100 ms is the average time for human hand–eye coordination [5]. With a 100 ms image feedback cycle, the operator is expected to be able to respond in a timely manner. However, with a control cycle of TR = 30 ms, the position of the robot can be refreshed more frequently to allow the operator to have better control over its motion.

Additionally, a control group was established for comparison. For this control group, the same experiments were conducted using conventional techniques for MRI navigation, as shown in Video S3 in Appendix A. Owing to the high degree of redundancy inherent in the image signals acquired through conventional methods, the control TR was constrained to a duration of approximately hundreds of milliseconds. Furthermore, the artifact sizes were up to 20 times the diameter of the particle itself, seriously affecting the image quality. Navigation in 3D was also found to be infeasible because of the reliance of conventional methodologies on 2D imaging.

3.2. In vitro *demonstration of phantom endovascular navigation*

Given the relatively simple structure of the maze, the motion of the robot was predominantly linear. To more closely approximate the conditions of the biological environment, we conducted a real-time demonstration experiment in a phantom vessel (Fig. 7(a)). Rapid steering through tortuous vessels is an essential function of magnetic robots, and the timely acquisition of image feedback is crucial for its effective execution [5]. Our MFDE sequence operates at a TR = 30 ms, offering a distinctive advantage.

The phantom 3D vessel model is composed of three sections (Fig. 7(b)). The first section consists of a plastic tube, which simulates a vessel. The second component is the base, which features numerous sockets on its surface and was crafted together with the third component: columns with rings of varying heights that can be affixed to the base via sockets. The tube can be threaded through the upper rings. Based on the configuration of the sockets, replicating diverse vascular pathways through the tube is feasible. The base and columns were 3D-printed using PLA materials. It is noteworthy that a gradient force in the +*Z*-direction is applied to the magnetic robot as the examination bed is pushed into the MRI region owing to the presence of a fringe field. To prevent unwanted robot movement during this process, an L-shaped turn was set up at the entrance of the maze to limit robot movement in the *Z*-direction.

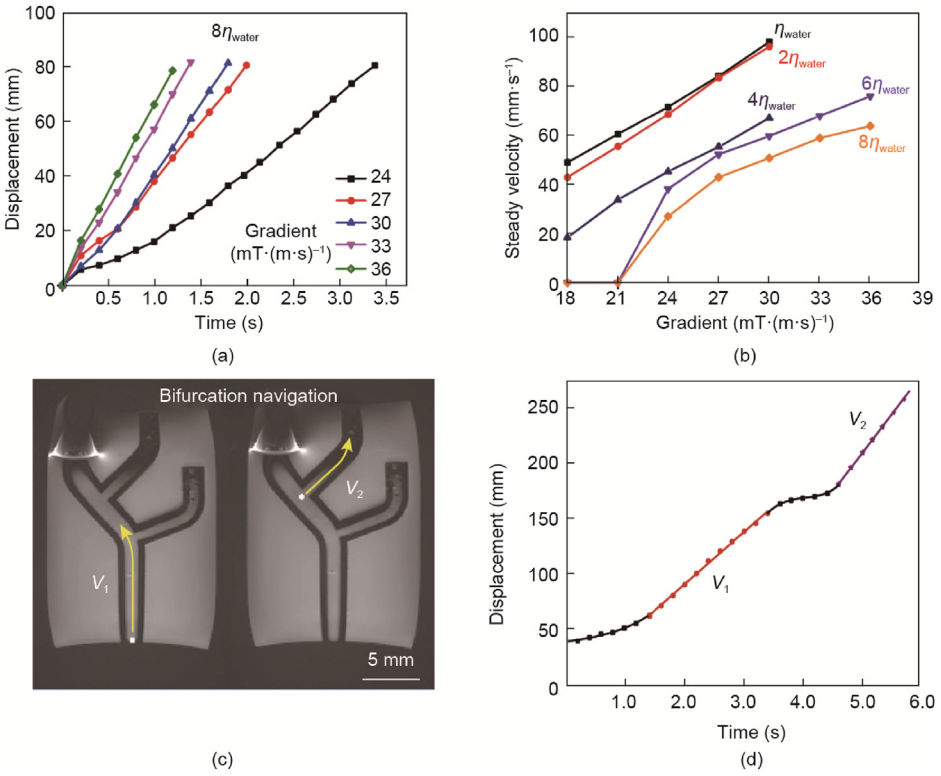

Fig. 5. Dynamic model of real-time and artifact-free MRI-navigation. (a) Displacement curves of magnetic particles under different magnetic gradient fields in fluids with viscosities eight times that of water. (b) Steady velocities in fluids with different viscosities under different gradients. η_{water}: water viscosity. (c, d) Magnetic particle travels through bifurcated paths at (c) different velocities (V_1 and V_2) and (d) corresponding curve.

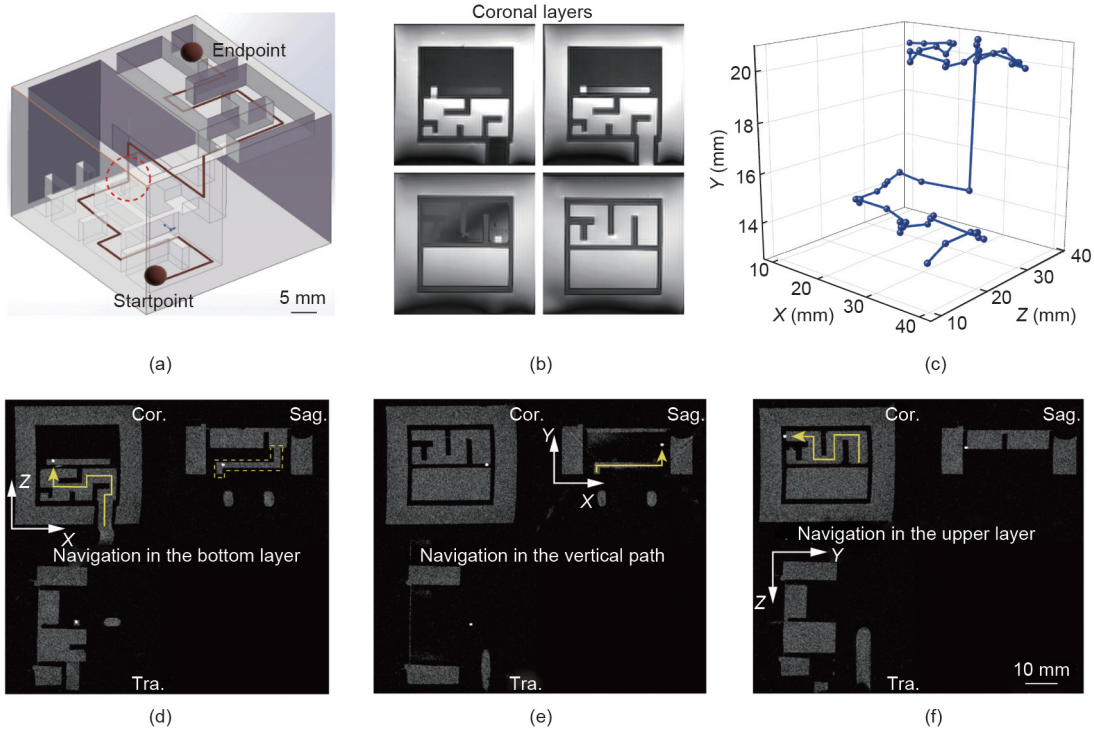

Fig. 6. Results of real-time open-loop maze navigation using integrated imaging-control platform. (a) 3D maze structure and predetermined route. Dotted area indicates entrance to vertical channel. (b) Coronal views of maze from bottom to top during passage of magnetic robot through the vertical path. A 2D image of each section is obtained by pre-background scanning, and 3D control is realized by refreshing the three views according to the position of the robot in real time. (c) Calculated 3D path analysis of magnetic robot. (d–f) Magnetic robot navigation in the (d) bottom layer, where dotted area marks the vertical channel, (e) vertical path, and (f) upper layer of the maze. Image resolution = 128 × 128 × 128 pixels. FOV = 50 mm × 50 mm × 50 mm.

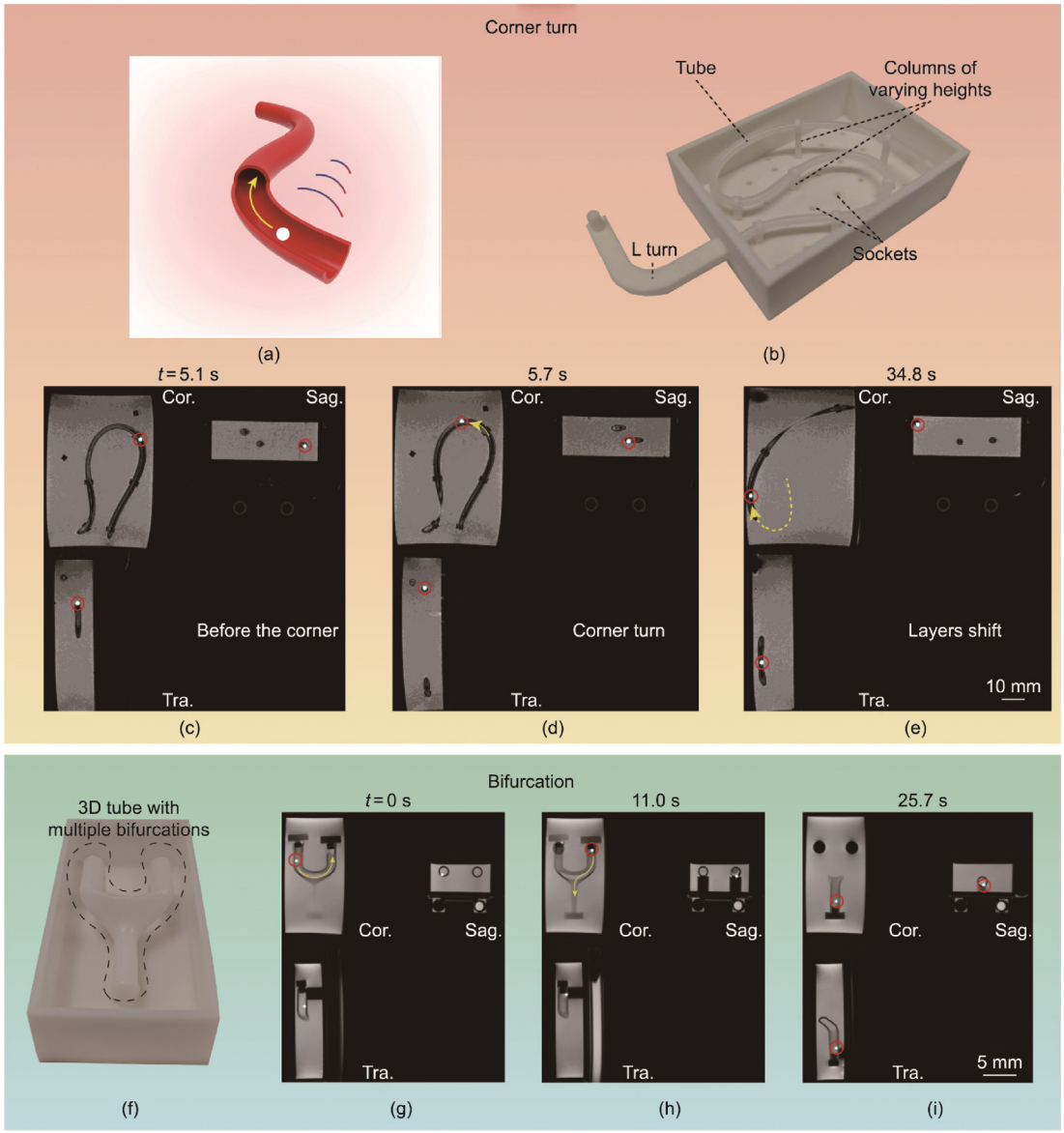

Fig. 7. Results of phantom endovascular navigation. (a) Schematic of magnetic navigation in vessel. (b) A phantom vessel with shape can be arbitrarily designed with different settings for the tube, columns with rings of varying heights, and sockets. The L-shaped turn is designed to prevent damage caused by the gradient force in the +*Z*-direction as the examination bed is pushed inward. (c–e) Navigating the magnetic robot inside the vessel. The robot can be steered to turn around in 0.6 s. As the robot moves deep into the phantom blood vessel, the three views centered on its position are refreshed in real time; thus, the different layers of the blood vessel in the three-view images shift in turn. The moments corresponding to each figure are labeled. Red dots indicate the position of the magnetic robot at various points in time as observed in the coronal image. Arrows indicate the navigation direction. (f) 3D phantom vessel with bifurcations. (g–i) Navigation between bifurcations. Image resolution = 192 × 192 × 192 pixels. FOV = 70 mm × 70 mm × 70 mm.

The phantom was filled with a liquid with a viscosity three times that of water. Then, the reconstructed 3D background image was fixed. Once the aforementioned steps had been completed, the magnetic robot was inserted through the entrance. To guarantee the precision of tracking, the voxel of the pre-obtained background image was calibrated to approximately 0.38 mm (a value smaller than the diameter of the magnetic particle), and thus, the FOV was set to 70 mm × 70 mm × 70 mm, and the corresponding resolution was set to 192 × 192 × 192 pixels.

Implementing rapid control-imaging feedback and regulated velocity helps the operator avoid violent friction or sharp injuries to the phantom vessel wall during the movement of the magnetic robot—particularly important to ensure the highest level of safety during surgical procedures. Moreover, the spherical shape of the robot reduces the potential for frictional damage to the phantom vessel. Figs. 7(c)–(e) depict the three-view feedback image of the robot as it progresses deeper into the tube. Here, the TR was designed to be as low as 30 ms, better than the recognition time of the human eye. Because the vascular pathway is complex and narrow, high-frame-rate image feedback is required for navigating the vasculature to ensure precise control. The time interval between Figs. 7(c) and (d) was 0.6 s, which suggests that the magnetic robot was steered to execute a corner turn with remarkable fluidity (Video S4 in Appendix A).

Further experiments were conducted in a 3D phantom blood vessel with bifurcations, as illustrated in Figs. 7(f)–(i). In such environments, overcoming environmental interference in imaging and localization is crucial. Our technology provides accurate localization and control capabilities, demonstrating stable control performance (Video S5 in Appendix A).

3.3. In vivo *demonstration of navigation in rat large intestine*

A navigation demonstration was also conducted on live animals. The rats used in the animal experiments were procured from Wuhan Hualianke Biotechnology Co., Ltd. (China), and the animal experiments were conducted according to the Institutional Animal Care and Use Committee of Huazhong Science and Technology (China).

Colorectal cancer and inflammatory bowel disease are the most prevalent intestinal disorders. The most effective means of preventing and treating these conditions is colonoscopy, which should be performed several times a year [30]. Considering the discomfort and potential safety concern associated with commonly used colonoscopies, considering the use of robotics for diagnostic and therapeutic integration is logical (Fig. 8(a)). A principal criterion for determining the viability of wireless magnetic robots as a replacement for colonoscopy is their capacity to gain access to the interior of the colon through the rectum and to return promptly, thereby ensuring safety for the patient.

Because of the tortuous passages in the intestine and the complex variety of substances therein, both MRI and motion control are seriously hindered. To address this problem, in this animal study, the rats were pretreated with enemas before the experiment. Subsequently, 3D background imaging of the gut was performed using the FSE sequence (Fig. 8(b)). This examination was done to provide

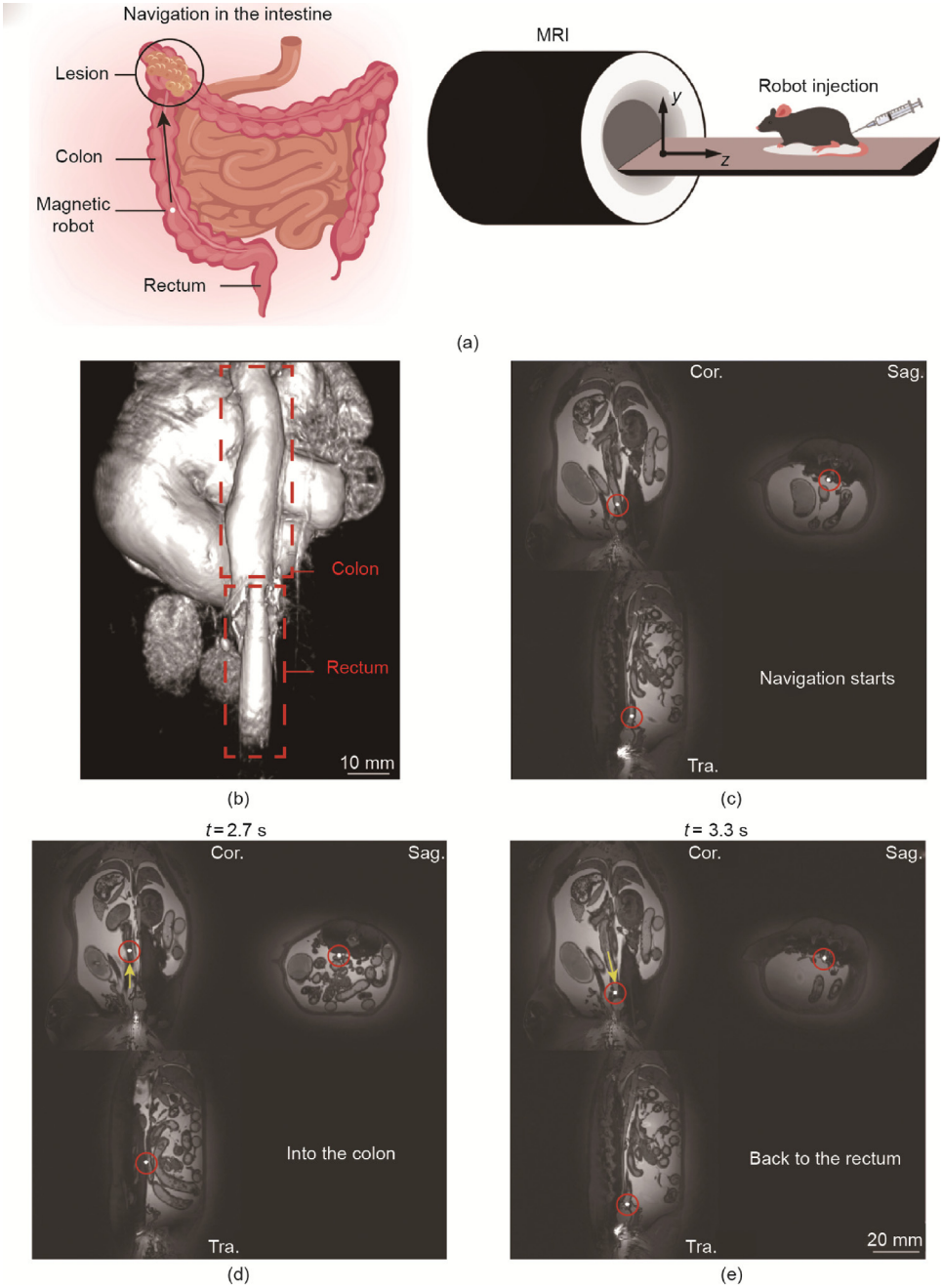

Fig. 8. Results of navigation in rat large intestine. (a) Schematic of MRI-driven robot for theranostics of intestinal lesions. Arrows indicate navigation of robot toward the lesion. (b) Pre-scan of 3D structure of large intestine. (c–e) Magnetic robot was delivered from the anus and navigated to move from (c) rectum to (d) colon and (e) return in 0.6 s. Each figure is appropriately labeled with the corresponding moments shown. Red dots indicate position of magnetic robot at various points in time as observed in coronal images. Arrows indicate navigation direction. Image resolution = 256 × 256 × 256 pixels. FOV = 90 mm × 90 mm × 90 mm.

a prior understanding of the structure of the deep gut. Given the complex interlacing of the intestines, the structure of the gut should be sufficiently clear to ensure safety as the robot penetrates deeply into the human body. After the examination bed was pushed in, the robot was steered into the anus of the rat. Subsequently, the robot was directed to traverse the rectum (Fig. 8(c)) and proceed to the colon (Fig. 8(d)). The distance between the rectum and colon was approximately 20 mm. The MFDE sequence was employed for the process, throughout which the real-time position was transmitted via a reconstructed light spot (TR = 30 ms). The continuous refreshing of the three views with the real-time position of the robot provided feedback from the *in vivo* environment, thereby helping ensure safety. Based on experience and real-time situations, the magnitude and direction of the applied force can be determined as required. The robot was demonstrated to reach the deep interior of the body. To prevent the implant from remaining in the body for an extended period, the magnetic robot was subsequently directed to return from the colon to the rectum (Fig. 8(e)). The average internal diameter of the rat intestine is less than 2.5 mm, which represents a significant limitation with respect to both the size of the robot and the accuracy of the control. The results of this test suggest that our proposed method has the potential to replace traditional colonoscopy as an alternative medical examination procedure that offers the same diagnostic benefit while eliminating patient discomfort and, thus, consequently, helping encourage patients undergo their recommended medical check-ups that could help save their lives (Video S6 in Appendix A).

3.4. Discussion

This study presents a solution to the inherent contradiction between background image quality and imaging speed in MRI-driven robotics [8]. Specifically, this contradiction is overcome through an integrated imaging-control sequence design with a 30 ms period. Our technique has demonstrated an order-of-magnitude breakthrough in TR and the removal of artifacts, thereby achieving high-resolution structural imaging and precise tracking, which represents a significant innovation over previous studies (Table 1 [9,23,25,27,28]).

Considering the ongoing advancement in medical devices and the growing demand for medical care, an increasing number of open surgeries are being supplanted by interventional procedures [31–33]. MRI systems that facilitate the navigation and manipulation of microrobots offer substantial promise for enhancing patient outcomes while diminishing procedural trauma. Furthermore, the adoption of soft-tissue imaging and the effective use of the magnetic control capabilities of MRI provide an efficacious alternative to conventional X-ray-based techniques. This non-invasive attribute is particularly advantageous for patients, especially in scenarios requiring repetitive procedures, because it obviates the risk of cumulative radiation exposure, a concern that has ignited considerable debate within the medical imaging community [34,35]. The real-time nature of our proposed navigation system allows robotic tasks to be accomplished in a matter of minutes. We demonstrated a colonoscopy alternative that navigates the robot to the target area within seconds. This method simultaneously avoids the background changes caused by intestinal peristalsis. By contrast, interventional procedures often last for several hours, sometimes even more than ten hours. Our technology demonstrates the possibility of an effective alternative approach that offers a more comfortable experience for the patient.

An increasing number of researchers have focused on the functionality of magnetic robots. Several research initiatives have been proposed with the objective of performing a diverse array of sophisticated medical procedures, including magnetic hyperthermia [3], vascular embolization [2], sensing [36–38], and controlled drug delivery [1,4,6,39–41]. For MRI systems, the energies stored in their strong magnetic fields have been overlooked and even criticized for their potential dangers, such as the inability to perform an MRI scan in patients with metal implants in their bodies. Nevertheless, future advancements are expected facilitate the further development and improvement of MRI-driven robots that integrate diagnostic and therapeutic functions. Furthermore, we aim to extend this work to all clinical departments.

4. Conclusions

This paper presents a RF field-based method for acquiring magnetic feature signals for real-time MRI-driven robot navigation with a TR = 30 ms. This method overcomes steady-state limitations by introducing a new MRI sequence in which positive and negative offset frequencies are excited alternately. Furthermore, using two adjacent 180° RF echoes accelerates the proton spin recovery process. Complemented by 3D projection, we achieved precise tracking with a relative error of < 1% on a pre-imaged artifact-free background. In conjunction with this proposed method, we also developed a three-view feedback and joystick control platform. We presented demonstrations of navigation in a maze, in a phantom vessel, and in a rat large intestine. Providing an open-loop imaging control system with a cyclic period as low as 30 ms is crucial, given that the human hand–eye coordination time is approximately 100 ms [26]. The results reported herein are expected to drive the translation of MRI-driven robotic surgery in clinical settings.

CRediT authorship contribution statement

Renkuan Zhai: Methodology. **Zhangqi Pan:** Writing – original draft. **Yuanshi Kou:** Validation. **Chuang Yang:** Software. **Yang Ruan:** Resources. **Chenli Xu:** Visualization. **Linjie He:** Resources. **Jianfeng Zang:** Conceptualization.

Declaration of competing interest

The authors declare that they have no known competing financial interests or personal relationships that could have appeared to influence the work reported in this paper.

Table 1
Comparison with conventional MRI sequences.

Ref.	TR (ms)	Artifacts	Duty cycle	Dimensions	Sequence
Zhang et al. [28]	> 1000	Presence	40%	2	FLASH
Latulippe et al. [9]	800	Presence	Not mentioned	2	SE
Erin et al. [25]	750	Presence	66.7%	2	RARE
Tamaz et al. [23]	480	Presence	40%	2	Echo Planar Imaging (EPI)
Fischer and Rogal [27]	350	Presence	70%	2	FLASH
This work	**30**	**Free**	**77%**	**3**	**MFDE**

Acknowledgments

This work was funded by the National Natural Science Foundation of China (T2350001 and 52173280), the Huazhong University of Science and Technology (HUST) Interdisciplinary Research Project (2023JCYJ044), and the Taihu Lake Innovation Fund for Future Technology, HUST (2023A3).

Appendix A. Supplementary data

Supplementary data to this article can be found online at https://doi.org/10.1016/j.eng.2025.04.027.

References:

[1] Li JY, Li XJ, Luo T, Wang R, Liu CC, Chen SX, et al. Development of a magnetic microrobot for carrying and delivering targeted cells. Sci Robot 2018;3(19):eaat8829.
[2] Liu XR, Wang L, Xiang YZ, Liao F, Li N, Li JY, et al. Magnetic soft microfiberbots for robotic embolization. Sci Robot 2024;9(87):eadh2479.
[3] Baker RR, Payne C, Yu YC, Mohseni M, Connell JJ, Lin FY, et al. Image-guided magnetic thermoseed navigation and tumor ablation using a magnetic resonance imaging system. Adv Sci 2022;9(12):2105333.
[4] Wang QQ, Chan KF, Schweizer K, Du XZ, Jin DD, Yu SCH, et al. Ultrasound doppler-guided real-time navigation of a magnetic microswarm for active endovascular delivery. Sci Adv 2021;7(9):eabe5914.
[5] Kim YH, Parada GA, Liu SD, Zhao XH. Ferromagnetic soft continuum robots. Sci Robot 2019;4(33):eaax7329.
[6] Go G, Jeong SG, Yoo A, Han J, Kang B, Kim S, et al. Human adipose-derived mesenchymal stem cell-based medical microrobot system for knee cartilage regeneration *in vivo*. Sci Robot 2020;5(38):eaay6626.
[7] Erin O, Boyvat M, Tiyraki ME, Phelan M, Sitti M. Magnetic resonance imaging system–driven medical robotics. Adv Intell Syst 2020;2(2):1900110.
[8] Tiryaki M, Sitti M. Magnetic resonance imaging-based tracking and navigation of submillimeter-scale wireless magnetic robots. Adv Intell Syst 2021;4(4):2100178.
[9] Latulippe M, Felfoul O, Dupont PE, Martel S. Enabling automated magnetic resonance imaging-based targeting assessment during dipole field navigation. Appl Phys Lett 2016;108:062403.
[10] Felfoul O, Mathieu JB, Beaudoin G, Martel S. *In vivo* MR-tracking based on magnetic signature selective excitation. IEEE Trans Med Imaging 2008;27(1):28–35.
[11] Folio D, Dahmen C, Wortmann T, Zeeshan A, Shou KY, Pané S et al. MRI magnetic signature imaging, tracking and navigation for targeted micro/nano-capsule therapeutics. In: Proceedings of the 2011 IEEE/RSJ International Conference on Intelligent Robots and Systems; 2011 Sep 25–30; San Francisco, CA, USA. Piscataway: IEEE; 2011. p. 1297–303.
[12] Mathieu JB, Martel S. Steering of aggregating magnetic microparticles using propulsion gradients coils in an MRI scanner. Magn Reson Med 2010;63(5):1336–45.
[13] Azizi A, Tremblay CC, Gagne K, Martel S. Using the fringe field of a clinical MRI scanner enables robotic navigation of tethered instruments in deeper vascular regions. Sci Robot 2019;4(36):eaax7342.
[14] Dahmen C, Belharet K, Folio D, Ferreira A, Fatikow S. MRI-based dynamic tracking of an untethered ferromagnetic microcapsule navigating in liquid. Int J Optomechatronics 2016;10(2):73–96.
[15] Folio D, Ferreira A. Two-dimensional robust magnetic resonance navigation of a ferromagnetic microrobot using pareto optimality. IEEE Trans Robot 2017;33(3):583–93.
[16] Martel S, Mathieu JB, Felfoul O, Chanu A, Aboussouan E, Tamaz S, et al. Automatic navigation of an untethered device in the artery of a living animal using a conventional clinical magnetic resonance imaging system. Appl Phys Lett 2007;90:114105.
[17] Felfoul O, Becker A, Bergeles C, Dupont PE. Achieving commutation control of an MRI-powered robot actuator. IEEE Trans Robot 2015;31(2):387–99.
[18] Chanu A, Felfoul O, Beaudoin G, Martel S. Adapting the clinical MRI software environment for real-time navigation of an endovascular untethered ferromagnetic bead for future endovascular interventions. Magn Reson Med 2008;59(6):1287–97.
[19] Tabatabaei SN, Lapointe J, Martel S. Shrinkable hydrogel-based magnetic microrobots for interventions in the vascular network. Adv Robot 2016;25(8):1049–67.
[20] Bilgin MB, Tiyaki ME, Lazovic J, Sitti M. Radio frequency sensing-based *in situ* temperature measurements during magnetic resonance imaging interventional procedures. Adv Mater Technol 2022;7(9):2101625.
[21] Tamaz S, Martel S. Impact of the MRI-based navigation system constraints on the step response using a PID controller. In: Proceedings of the 2005 IEEE Engineering in Medicine and Biology 27th Annual Conference; 2006 Jan 17–18; Shanghai, China. Piscataway: IEEE; 2006. p. 5073–6.
[22] Tamaz S, Gourdeau R, Martel S. Bidimensional MRI-based navigation system using a PID controller. In: Proceedings of the 2006 International Conference of the IEEE Engineering in Medicine and Biology Society; 2006 Aug 30–Sep 03; New York City, USA. Piscataway: IEEE; 2016. p. 4424–7.
[23] Tamaz S, Gourdeau R, Chanu A, Mathieu JB, Martel S. Real-time MRI-based control of a ferromagnetic core for endovascular navigation. IEEE Trans Biomed Eng 2008;55(7):1854–63.
[24] Tiryaki ME, Erin Ö, Sitti M. A realistic simulation environment for MRI-based robust control of untethered magnetic robots with intra-operational imaging. IEEE Robot Autom Lett 2020;5(3):4501–8.
[25] Erin O, Antonelli D, Tiryaki ME, Sitti M. Towards 5-DoF control of an untethered magnetic millirobot via MRI gradient coils. In: Proceedings of the 2020 IEEE International Conference on Robotics and Automation (ICRA); 2020 May 31–Aug 31; Paris, France. Piscataway: IEEE; 2020. p. 6551–7.
[26] Erin O, Boyvat M, Lazovic J, Tiryaki EM, Sitti M. Wireless MRI-powered reversible orientation-locking capsule robot. Adv Sci 2021;8(13):2100463.
[27] Fischer B, Rogal L. Eye-hand-coordination in man: a reaction time study. Biol Cybern 1986;55:253–61.
[28] Zhang K, Krafft AJ, Umathum R, Maier F, Semmler W, Bock M. Real-time MR navigation and localization of an intravascular catheter with ferromagnetic components. Magn Reson Mater Phy Biol Med 2010;23:153–63.
[29] Folio D, Ferreira A. Two-dimensional robust magnetic resonance navigation of a ferromagnetic microrobot using pareto optimality. IEEE Trans Robot 2017;33:583–93.
[30] Hommes DW, van Deventoer SJH. Endoscopy in inflammatory bowel diseases. Gastroenterology 2004;126(6):1561–73.
[31] Kinross JM, Mason SE, Mylonas G, Darzi A. Next-generation robotics in gastrointestinal surgery. Nat Rev Gastroenterol Hepatol 2020;17:430–40.
[32] Ray K. Autonomous robotic laparoscopic gastrointestinal surgery. Nat Rev Gastroenterol Hepatol 2022;19:148.
[33] Lobo MD, Sobotka PA, Pathak A. Interventional procedures and future drug therapy for hypertension. Eur Heart J 2017;38(15):1101–11.
[34] Cusma JT, Bell MR, Wondrow MA, Taubel JP, Holmes DR. Real-time measurement of radiation exposure to patients during diagnostic coronary angiography and percutaneous interventional procedures. J Am Coll Cardiol 1999;33(2):427–35.
[35] Li ZY, Li J, Wu ZH, Chen YH, Yeerbulati M, Xu QS. Design and hierarchical control of a homocentric variable-stiffness magnetic catheter for multiarm robotic ultrasound-assisted coronary intervention. IEEE Trans Robot 2024;40:2306–26.
[36] Hr Gu, Möckli M, Ehmke C, Kim MS, Wieland M, Moser S, et al. Self-folding soft-robotic chains with reconfigurable shapes and functionalities. Nat Commun 2023;14:1263.
[37] Yan YC, He Z, Yang ZB, Yuan WZ, Song CY, Pan J, et al. Soft magnetic skin for super-resolution tactile sensing with force self-decoupling. Sci Robot 2021;6(51):eabc8801.
[38] Dong Y, Wang L, Xia N, Yang ZX, Zhang C, Pan CF, et al. Untethered small-scale magnetic soft robot with programmable magnetization and integrated multifunctional modules. Sci Adv 2022;8(25):eabn8932.
[39] Zhang YM, Liu F, Zhang YH, Wang J, D'Andrea D, Walter JB, et al. Self-powered, light-controlled, bioresorbable platforms for programmed drug delivery. Proc Natl Acad Sci USA 2023;120(11):e2217734120.
[40] Wang QL, Wang QQ, Ning ZP, Chan KF, Jiang JL, Su L, et al. Tracking and navigation of a microswarm under laser speckle contrast imaging for targeted delivery. Sci Robot 2024;9(87):eadh1978.
[41] Wang QQ, Du XZ, Jin DD, Zhang L. Real-time ultrasound doppler tracking and autonomous navigation of a miniature helical robot for accelerating thrombolysis in dynamic blood flow. ACS Nano 2022;16(1):604–16.